THE JOURNAL OF PHYSICAL CHEMISTRY C
A JOURNAL OF THE AMERICAN CHEMICAL SOCIETY

pubs.acs.org/JPCC

Article

$Nb_6Mn_{1-x}Ir_{6+x}B_8$ (x = 0.25): A Ferrimagnetic Boride Containing Planar B_6 Rings Interacting with Ferromagnetic Mn Chains

Published as part of The Journal of Physical Chemistry virtual special issue "Alexander Boldyrev Festschrift".

Neetika Sharma, Yuemei Zhang, Mohammed Mbarki, Jan P. Scheifers, Kunio Yubuta, Simon A. J. Kimber, and Boniface P. T. Fokwa*

Cite This: *J. Phys. Chem. C* 2021, 125, 13635−13640

Read Online

ACCESS | Metrics & More | Article Recommendations | Supporting Information

ABSTRACT: Discovering new low-dimensional magnetic materials is of paramount importance in spintronics. We report on a new ferrimagnetic (FiM) compound, $Nb_6Mn_{1-x}Ir_{6+x}B_8$ (x = 0.25), the structure of which contains Mn chains embedded in stacked planar B_6 rings. Its crystal structure, which was determined by combined single-crystal X-ray and neutron diffraction studies, contains three Mn chains (intrachain distance is 3.30 Å) building a triangular network with an interchain distance of 9.28 Å, indicating stronger intrachain interactions than interchain ones. Density functional theory (DFT) calculations proposed ferrimagnetic ordering for the new phase resulting from three nonequivalent, triangularly arranged ferromagnetic (FM) Mn chains with two in spin-up and one in spin-down. Magnetization measurements confirmed the presence of not only strong FM interactions (high Curie temperature of 250 K) but also weak antiferromagnetic (AFM) ones (small and negative Weiss constant of −70 K), thus confirming the proposed FiM ordering.

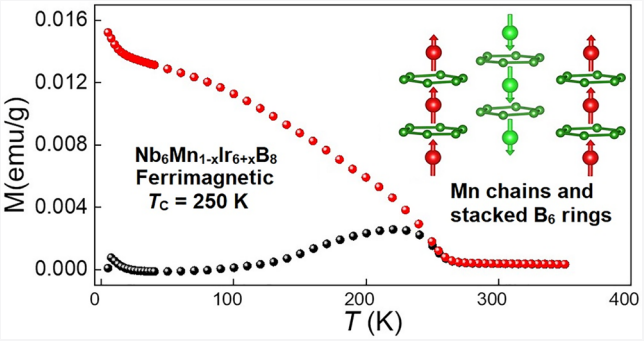

INTRODUCTION

Crystalline transition metal borides constitute a large group of intermetallic materials that have provided some of the most important materials that are relevant to our modern society.[1−3] As such, they have been the focus of recent fundamental research in areas such as hard and superhard materials, thermoelectrics, catalysts, and superconducting, magnetocaloric, and magnetic materials, just to name a few.[4−12] Among these materials, magnetic transition metal borides are part of the subgroup of metal-rich borides which adopt a variety of crystal structures with different arrangements of boron atoms within a 3D network of metals. Such metal-rich structures are mostly characterized by the presence of not only isolated boron atoms (no B−B bonds) but also small boron fragments (B_n). Boldyrev and Wang pioneered the discovery of planar boron fragments in the gas phase and predicted that they could not only lead to the discovery of new molecular and solid-state compounds but also impact their electronic and physical properties.[13] Indeed, a few years ago, we discovered an unexpected synergy between planar B_6 rings and chains of iron atoms that directly impacted the magnetic behavior of $Nb_6Fe_{1-x}Ir_{6+x}B_8$.[14] Chemical bonding analysis (via spin-polarized calculations) showed that the presence of long-range ferromagnetic interactions within the Fe chain strengthens the already strong B−B interactions even more, thereby enhancing the stability of the compound and favoring magnetic ordering simultaneously. $Nb_6Fe_{1-x}Ir_{6+x}B_8$ was synthesized by an extremely quick arc-melting procedure, which hinted at a possible kinetic phase. Annealing of the arc-melted compound leads to the formation of a thermodynamically stable $\sqrt{3} \times \sqrt{3} \times 2$ superstructure (space group $P6/m$)[15] in which structural distortions led to the discovery of the first ferrimagnetic iron chain in intermetallic compounds. Several questions emerged from these works: (1) Are these discoveries unique to this compound or are other isotypic compounds as capable, and (2) does the interplay of kinetic and thermodynamic stabilities exist for other compounds?

In the quest to investigate the role of different magnetic elements on the stability of the kinetically stabilized structure and further on the magnetic properties, we have substituted Fe by another magnetic 3d element, Mn. Using the same synthetic strategy as for the $Nb_6FeIr_6B_8$ (quick arc melting), we have synthesized crystalline sample of isotypic $Nb_6MnIr_6B_8$, whose

Received: March 24, 2021
Revised: May 30, 2021
Published: June 9, 2021

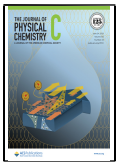

https://doi.org/10.1021/acs.jpcc.1c02662
J. Phys. Chem. C 2021, 125, 13635−13640

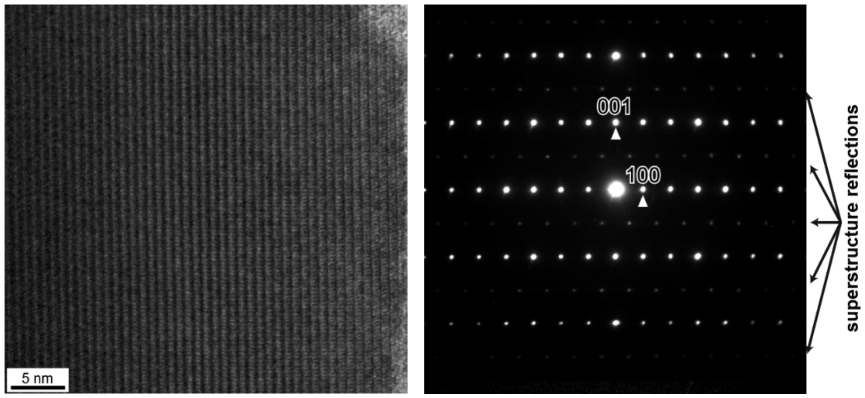

Figure 1. HRTEM image of an arc-melted sample of $Nb_6MnIr_6B_8$ (left) and the corresponding selected area electron diffraction pattern (right) showing weak superstructure reflections which indicate the doubling of the *c* lattice parameter.

diffraction experiments unexpectedly showed the 6-fold ($\sqrt{3} \times \sqrt{3} \times 2$) superstructure reflections found for $Nb_6FeIr_6B_8$ after annealing. Density functional theory (DFT) calculations then proposed ferrimagnetic ordering resulting from antiferromagnetic interactions of three triangularly arranged ferromagnetic Mn chains, in contrast to the ferrimagnetic Fe chains in annealed $Nb_6FeIr_6B_8$. Magnetization measurements confirmed the ferrimagnetic ordering below T_c = 250 K for the new phase.

RESULTS AND DISCUSSION

The new phase was synthesized by a quick arc-melting procedure of stoichiometric amounts of the elemental powders (see ref 16 for more details). The synthesized polycrystalline product contained small single crystals that could be isolated for X-ray diffraction (XRD) studies. Single-crystal XRD data showed not only strong substructure reflections but also weak superstructure ones, which were further confirmed by high-resolution transmission electron microscopy (HRTEM) and its diffraction image (Figure 1). Two refinement models were developed by using the substructure on the one hand and adding the superstructure reflections on the other. Structure refinement using the substructure reflections converged smoothly (see the Supporting Information Tables S1 and S2) after refining 25% Ir on the Mn site ($Nb_6Fe_{1-x}Ir_{6+x}B_8$ model[14] but replacing Fe by Mn), leading to the composition $Nb_6Mn_{0.75(2)}Ir_{6.25(2)}B_8$. Furthermore, the powder data not only confirmed the single-crystal results but also proved the presence of side phases in the sample (also confirmed by neutron diffraction results below), and qualitative energy dispersive X-ray spectroscopy (EDS) confirmed the presence of all metals in the analyzed single crystal (Figure S1).

A second model was then developed considering the superstructure reflections ($\sqrt{3} \times \sqrt{3} \times 2$ superstructure, space group *P6/m*), and it turned out to be identical with that of annealed $Nb_6FeIr_6B_8$. However, the very weak superstructure reflections led to high *R*-values for the refinement; thus, we performed neutron powder diffraction (NPD) to verify this superstructure model, as it is crucial in understanding the magnetic properties. NPD patterns were recorded at 300 and 13 K, as exemplified in Figure 2 showing a section of a typical NPD pattern at 300 K. For the NPD refinement of $Nb_6FeIr_6B_8$, it was not possible to model the Fe/Ir mixed occupancy properly because of the similar neutron scattering lengths of Fe and Ir. Consequently, the NPD data were refined by considering full Fe occupancy at all Fe sites. However, for

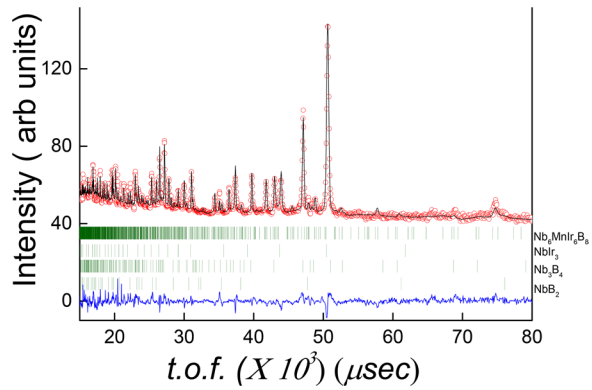

Figure 2. Observed (red circles) and calculated (black line) powder neutron diffraction patterns for $Nb_6MnIr_6B_8$ at 300 K. Lower solid blue line is the difference between observed and calculated patterns. The first row of tick marks indicates the position of nuclear Bragg peaks for $Nb_6MnIr_6B_8$ (space group *P6/m*), and the second, third, and fourth rows of tick marks indicate the Bragg peaks positions for the side phases $NbIr_3$, Nb_3B_4, and NbB_2, respectively.

the Mn compound, we can study the mixed occupancies because of the different neutron scattering lengths of Mn and Ir. We first tried the structure model with full Mn occupancies at all Mn sites, but the refinement did not converge. Then we tried successively refining mixed occupancies; initially at each of the four Mn positions (Wyckoff sites 1a, 1b, 2c, and 2d), then up to three sites could be refined simultaneously but not all four sites. The resulting mixed occupancy refinements led to a significant variation of the Ir amount in each site depending on the number of sites refined simultaneously. Interestingly, the average variation of the Ir content on these Mn sites turned out to be closer to the amount obtained from the single-crystal substructure refinement (25%). Furthermore, fixing the Mn/Ir content to the refined single-crystal values of 75/25% on all Mn sites did not change the *R*-values obtained from the best mixed-occupancy refinements. Therefore, the final NPD refinement data (Table 1 and Tables S3−S5) were based on this model which incorporates the refined composition from the single-crystal substructure refinement, $Nb_6Mn_{0.75(2)}Ir_{6.25(2)}B_8$. Both powder XRD and neutron diffraction have indicated the presence of the expected main phase (ca. 77%) along with side phases $NbIr_3$, Nb_3B_4, and NbB_2 (Figure 2). The cell parameters, weight fractions of all the phases, and the agreement factors obtained from Rietveld refinement of the neutron diffraction data at 300 and 13 K are

https://doi.org/10.1021/acs.jpcc.1c02662
J. Phys. Chem. C 2021, 125, 13635−13640

Table 1. Lattice Parameters, *R* Factors, and Weight Fractions of the Different Phases Obtained from Rietveld Refinement of the Powder Neutron Diffraction Data Are Given

temp (K)	13	300
a (Å)	16.1110(6)	16.1260 (6)
c (Å)	6.6092(4)	6.6185(4)
R_p	2.12	2.17
χ^2	5.31	13.2
space group, Z	*P6/m* (no. 175), 6	
$Nb_6Mn_{0.75}Ir_{6.25}B_8$ phase fraction (%)	77(2)	77(2)
side phase weight fraction $NbIr_3$, Nb_3B_4, NbB_2 (%)	18.0(4), 3.8(3), 1.1(3)	16.0(4), 4.7(3), 1.9(3)

given in Table 1. We have less Mn in the main phase than expected, and this is due to Mn loss observed during arc melting (low boiling point of Mn). Consequently, we do not expect any significant Mn in the side phases. The refined interatomic distances (Table S5) are consistent with those found in similar transition metal borides such as $Nb_6Fe_{1-x}Ir_{6+x}B_8$, $Sc_2MIr_5B_2$ (M = Mn, Fe), and the recently discovered $Hf_2MIr_5B_2$ phases (M = Fe, Mn).[16−18]

The refined crystal structure (Figure 3) of $Nb_6Mn_{0.75}Ir_{6.25}B_8$ is isotypic to that of annealed $Nb_6FeIr_6B_8$ phase[15] and contains

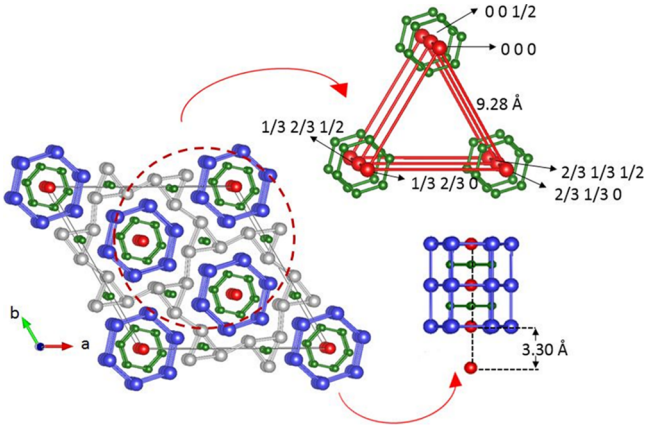

Figure 3. Perspective view along [001] of the crystal structure of $Nb_6MnIr_6B_8$. Triangular arrangement of Mn chains (top right) and part of the structure showing the layer-like arrangement along the *c*-direction (bottom right). Blue, red, gray, and green spheres represent Nb, Mn, Ir, and B atoms, respectively.

three chains of magnetic Mn atoms each built by two Wyckoff sites (one 1a/1b chain and two 2c/2d chains, Figure 3, top right). These Mn chains all have the exact same intrachain (*c*/2 = 3.30 Å) and interchain distances, but their coordination environments (distances around each Mn) are different (see Figure S2). The ferrimagnetic properties found in annealed $Nb_6FeIr_6B_8$ were attributed to the presence of similar chains but built by Fe atoms.[15] According to DFT calculations, strong antiferromagnetic (AFM) interactions exist within each of the three Fe chains, and because the two Wyckoff sites that build each chain have different magnetic moments (especially the 1a/1b Fe chain), the total moment did not cancel, leading to ferrimagnetic behavior.

Given the fact that elemental Mn shows strong AFM interactions if compared to the strong FM ones found in elemental Fe, it may be speculated that even stronger AFM interactions can be found in the new $Nb_6Mn_{0.75}Ir_{6.25}B_8$ phase if compared to the isotypic Fe-based one. We have therefore performed similar non-spin-polarized (nsp) and spin-polarized (sp) DFT calculations using the magnetic models applied to $Nb_6FeIr_6B_8$ but replacing Fe by Mn: one ferromagnetic model (FM) and four ferrimagnetic models (Fi1a, Fi1b, Fi2, and Fi3) which include the preferred model for $Nb_6FeIr_6B_8$ (Fi3). All five magnetic models were developed utilizing the experimentally observed structure at 13 K but with 100% Mn on all Mn sites (Figure 4). These models are (by at least 639 meV/

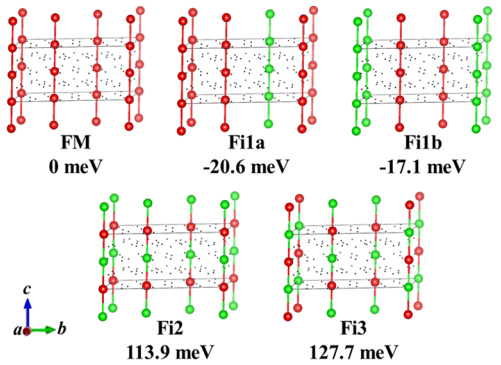

Figure 4. Magnetic models used for the DFT calculations for $Nb_6MnIr_6B_8$ and their corresponding energies relative to the ferromagnetic model (FM). Red and green spheres represent opposite spins on Mn atoms.

f.u.) far more energetically favorable than the nonmagnetic model, clearly pointing to long-range magnetic ordering in this new phase. The calculated magnetic moments on the four Mn atoms in the unit cell are all different from each other, even in the ferromagnetic model (see Table 2), and this is due to the different coordination environments around each of these four Mn sites (1a, 1b, 2c, and 2d), indicating that a full compensation of spins in an AFM arrangement in one chain is impossible, a behavior reminiscent of that found for $Nb_6FeIr_6B_8$. Surprisingly, we found that the magnetic intrachain Mn−Mn interactions are FM because the FM model is lower in energy than the Fi2 model which has intrachain AFM interactions, in strong contrast to the AFM intrachain Fe−Fe interactions found in $Nb_6FeIr_6B_8$.[15] However, out of the three triangularly arranged Mn chains, two in spin-up and one in spin-down are found in the most favorable magnetic models (Fi1a and Fi1b, see Figure 4 and Table 2), thereby predicting ferrimagnetic ordering for the new phase albeit with different models than that found in the Fe-based phase (Fi3). The difference between the two Fi1 models is minimal (only 3.5 meV/f.u. in favor of Fi1a), as in Fi1a one of the two 2c/2d Mn chains is spin-down while in Fi1b it is the 1a/1b Mn chain instead (Table 2). Importantly, the newly predicted magnetic models suggest dominating FM intrachain interactions but weaker AFM interchain interactions because the Fi1 models are lower in energy than the FM model. Because the spins of the triangularly arranged three FM Mn chains cannot be simultaneously aligned opposite to each other, the Fi1 models are adopted. Furthermore, because of the nonequivalence of the Mn chains, the resulting triangular geometry cannot lead to a frustrated system. It is worth mentioning that optimizing the atomic coordinates while fixing the volume and cell shape did not change the favorability of the magnetic model, as just slight energy changes occurred (Table S6).

https://doi.org/10.1021/acs.jpcc.1c02662
J. Phys. Chem. C 2021, 125, 13635−13640

Table 2. Calculated Energies and Magnetic Moments on Mn Atoms for Different Magnetic Models[a]

		moment on Mn (μ_B)						
		Mn1−Mn3 chain		Mn2−Mn4 chain		Mn2′−Mn4′ chain		
	energy (meV/f.u.)	Mn1 (000)	Mn3 ($00^1/_2$)	Mn4 ($^2/_3{}^1/_3 0$)	Mn2 ($^2/_3{}^1/_3{}^1/_2$)	Mn4′ ($^1/_3{}^2/_3 0$)	Mn2′ ($^1/_3{}^2/_3{}^1/_2$)	absolute total moment (μ_B/f.u.)
FM	0	3.274	3.257	3.041	3.156	3.041	3.156	3.536
Fi1a	−20.6	3.267	3.263	3.043	3.141	−3.054	−3.145	1.163
Fi1b	−17.1	−3.258	−3.269	3.052	3.163	3.052	3.163	1.209
Fi2	113.9	3.170	−3.265	2.750	−3.193	2.750	−3.193	0.222
Fi3	127.7	−3.216	3.254	2.675	−3.235	2.675	−3.235	0.317

[a]Energy differences are relative to the FM model. The calculations utilized experimentally observed structure at 13 K but with 100% Mn on all Mn sites.

We have performed SQUID measurements at low applied magnetic field (0.01 T) to verify these theoretical findings. Indeed, a Curie temperature (T_C) of ∼250 K was found (Figure 5), and a negative Weiss constant Θ ∼ −70 K was

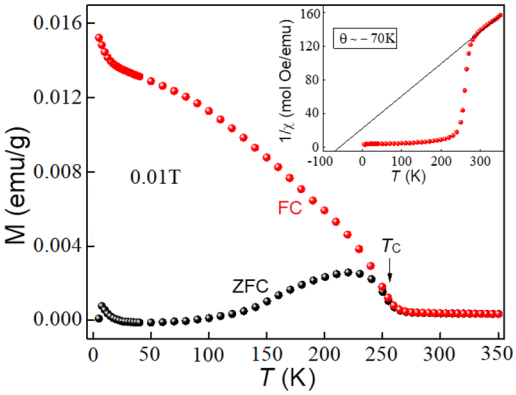

Figure 5. Temperature dependent ZFC and FC magnetization curves for $Nb_6MnIr_6B_8$ under an applied field of 0.01 T. Top inset (a) shows inverse of susceptibility ($1/\chi$) as a function of temperature and fit to the Curie−Weiss law (solid line).

obtained from the Curie−Weiss linear fit to the $1/\chi$ data in the temperature range 285−350 K. The $M-H$ curve at 5 K (Figure S3) shows a small hysteresis and a magnetic moment of 0.05 μ_B/f.u. (at 0.45 T); however, no saturation of the magnetization is achieved. Because the sample contains side phases (Table 1), there is a possibility that these phases can affect the magnetic ordering. However, as shown above, the side phases do not contain any significant amount of the magnetic element (Mn); thus, it is unlikely that they are magnetically ordered. Consequently, the magnetic ordering can be solely attributed to the main phase. The high Curie temperature clearly points to strong FM interactions (likely from intrachain Mn−Mn interactions) while the much smaller but negative value of the Weiss constant indicates the presence of weak antiferromagnetic interactions (likely from interchain Mn−Mn interactions) in the system. Therefore, this arc-melted nonannealed Mn-based sample orders ferrimagnetically as predicted. Another signature of ferrimagnetic ordering is the downward curvature of the $1/\chi-T$ curve at T_C. Furthermore, theory predicted a different ferrimagnetic model for the new phase than that of the previously reported annealed isotypic Fe-based phase: In fact, the two models have both AFM and FM interactions, but the Fe model has dominating AFM intrachain interactions while in the Mn model FM intrachain interactions are dominant. Indeed, the two phases have negative Weiss constants, but the Fe phase has a far larger value (−995 K) than that of the Mn phase, thus confirming much stronger AFM interactions in the former. Ferrimagnetism involving different multiplicities of two antiferromagnetically aligned Mn or Fe sites have been observed before in other material classes such as oxides, intermetallics, and chalcogenides.[19−22]

CONCLUSIONS

The new ferrimagnetic phase $Nb_6Mn_{0.75}Ir_{6.25}B_8$ was synthesized by arc-melting stoichiometric amount of the elements. The crystal structure, which was solved by combined single crystal X-ray diffraction and neutron diffraction studies, contains chains of Mn atoms interacting with planar B_6 rings. DFT calculations showed that the new compound orders ferrimagnetically due to strong FM intrachain interactions and weak AFM interchain interactions. SQUID measurements proved the ferrimagnetic ordering below 250 K with a negative Weiss constant of −70 K supporting the DFT results.

EXPERIMENTAL SECTION

Powder samples and needle-shaped silvery single crystals of title phase were synthesized by the arc-melting stoichiometric ratio of high-purity elements (at least 99.9%) in a water-cooled copper crucible under an argon atmosphere. For details concerning the synthetic steps see ref 16. Single-crystal X-ray diffraction data were collected on a Bruker SMART APEX CCD diffractometer with graphite-monochromatized Mo Kα radiation (λ = 0.71073 Å). The initial substructure solution and refinement were performed by means of the SHELX programs[23] (see Table S1). The crystallographic data collected for several single crystals provided identical chemical compositions, and the presence of all metals was confirmed by energy dispersive X-ray spectroscopy (EDS) analysis on several crystals analyzed on a high-resolution REM of the type Zeiss SUPRA 50 VP (Zeiss, Oberkochen, Germany) equipped with an EDS system of the type INCA (Oxford, England). The magnetization measurements were performed on a physical properties measurement system (PPMS) equipped with a superconducting quantum interference device (SQUID). The zero field and field cooled measurements were performed under a magnetic field of 0.01 T. Hysteresis loops were measured between −0.5 and +0.5 T at 5 K. The data were corrected for the sample holder (Teflon tubes). Powder samples of $Nb_6MnIr_6B_8$ for neutron diffraction studies were synthesized by using ^{11}B. Neutron diffraction patterns were collected at T = 13 and 300 K at the time-of-flight (TOF) neutron diffractometer by using the POWGEN instrument at Oak Ridge National Laboratory (ORNL).[24] The neutron

https://doi.org/10.1021/acs.jpcc.1c02662
J. Phys. Chem. C 2021, 125, 13635−13640

diffraction patterns were refined by the Rietveld method using the FULLPROF program.[25] Thin samples for transmission electron microscopy (TEM) observation were prepared by dispersing crushed materials on holey carbon films. Selected area electron diffraction patterns were obtained by using a 200 kV electron microscope (TOPCON EM-002B).

The *ab initio* calculations were performed by using the projector augmented wave (PAW) formalism of the Kohn–Sham density functional theory (DFT), as implemented in the *Vienna ab initio simulation package* (VASP).[26−29] A *k*-point mesh of 3 × 3 × 7, according to Monkhorst–Pack[30] scheme, was used for integration over the first Brillouin zone. The cutoff energy for the plane wave calculation was set to 500 eV. The total energies were obtained by solving the Kohn–Sham equations self-consistently within the generalized gradient approximation (GGA) of Perdew–Burke–Ernzerhof (PBE).[31] Both non-spin-polarized and spin-polarized calculations were performed. All results converged well with respect to k-mesh and energy cutoff for the plane-wave expansion. The structures were relaxed with respect to both lattice parameters and atomic positions. The convergence threshold for structural relaxation was set to be 0.02 eV/Å in force.

■ ASSOCIATED CONTENT

Supporting Information

The Supporting Information is available free of charge at https://pubs.acs.org/doi/10.1021/acs.jpcc.1c02662.

EDS spectrum, Mn coordination, magnetization vs *H* plot, crystallographic and structure refinement data, calculated energies and magnetic moments (PDF)

■ AUTHOR INFORMATION

Corresponding Author

Boniface P. T. Fokwa − *Department of Chemistry, University of California, Riverside, Riverside, California 92521, United States;* orcid.org/0000-0001-9802-7815; Email: bfokwa@ucr.edu

Authors

Neetika Sharma − *Department of Chemistry, University of California, Riverside, Riverside, California 92521, United States*

Yuemei Zhang − *Department of Chemistry, University of California, Riverside, Riverside, California 92521, United States;* orcid.org/0000-0003-1574-2931

Mohammed Mbarki − *Institute of Inorganic Chemistry, RWTH Aachen University, Aachen D-52074, Germany*

Jan P. Scheifers − *Department of Chemistry, University of California, Riverside, Riverside, California 92521, United States*

Kunio Yubuta − *Institute for Materials Research, Tohoku University, Sendai 980-8577, Japan*

Simon A. J. Kimber − *Neutron Sciences Division, Oak Ridge National Laboratory, Oak Ridge, Tennessee 37831, United States*

Complete contact information is available at: https://pubs.acs.org/10.1021/acs.jpcc.1c02662

Notes

The authors declare no competing financial interest.

■ ACKNOWLEDGMENTS

This work was supported by the startup fund to BPTF at UC Riverside and a partial support from the National Science Foundation Career award to BPTF (no. DMR-1654780). The San Diego Supercomputer Center (SDSC) is gratefully acknowledged for providing computing resources. The XPS data were collected with an instrument acquired through the NSF MRI program (DMR-0958796). A portion of this research used resources at the Spallation Neutron Source, a DOE Office of Science User Facility operated by the Oak Ridge National Laboratory. K.Y. was partly supported by JSPS KAKENHI under grant numbers JP19K05643 and JP20H05258.

■ REFERENCES

(1) Fokwa, B. P. T. Borides: Solid-state chemistry. In *Encyclopedia of Inorganic and Bioinorganic chemistry*; Scott, R. A., Ed.; John Wiley & Sons, Ltd.: 2014.

(2) Albert, B.; Hillebrecht, H. Boron: Elementary challenge for experimenters and theoreticans. *Angew. Chem., Int. Ed.* **2009**, *48*, 8640−8668.

(3) Akopov, G.; Yeung, M. T.; Kaner, R. B. Rediscovering the crystal chemistry of borides. *Adv. Mater.* **2017**, *29*, 1604506.

(4) Nagamatsu, J.; Nakagawa, N.; Muranaka, T.; Zenitani, Y.; Akimitsu, J. Superconductivity at 39 K in magnesium diboride. *Nature* **2001**, *410*, 63−64.

(5) Mori, T. Boron-based materials. In *Materials Aspect of Thermoelectricity*; Uher, C., Ed.; CRC Press: 2016.

(6) Park, H.; Encinas, A.; Scheifers, J. P.; Zhang, Y.; Fokwa, B. P. T. Boron-dependency of molybdenum borides electrocatalysts for the hydrogen evolution reaction. *Angew. Chem., Int. Ed.* **2017**, *56*, 5575−5578.

(7) Tan, X.; Chai, P.; Thompson, C. M.; Shatruk, M. Magnetocaloric effect in $AlFe_2B_2$: toward magnetic refrigerants from earth-abundant elements. *J. Am. Chem. Soc.* **2013**, *135*, 9553−9557.

(8) Levine, J. B.; Tolbert, S. H.; Kaner, R. B. Advancements in the Search for Superhard Ultra-Incompressible Metal Borides. *Adv. Funct. Mater.* **2009**, *19*, 3519−3533.

(9) Herbst, J. F.; Croat, J. J.; Pinkerton, F. E.; Yelon, W. B. Relationships between crystal structure and magnetic properties in $Nd_2Fe_{14}B$. *Phys. Rev. B: Condens. Matter Mater. Phys.* **1984**, *29*, 4176−4178.

(10) Scheifers, J. P.; Zhang, Y.; Fokwa, B. P. T. Boron: Enabling Exciting Metal-rich Structures and Magnetic Properties. *Acc. Chem. Res.* **2017**, *50*, 2317−2325.

(11) Mudgel, M.; Awana, V. P. S.; Kishan, H.; Felner, I.; Alvarez, G. A.; Bhalla, G. L. Superconductivity of various borides: The role of stretched c-parameter. *J. Appl. Phys.* **2009**, *105*, 07E313.

(12) Gabani, S.; Flachbart, K.; Siemensmeyer, K.; Mori, T. Magnetism and superconductivity of rare earth borides. *J. Alloys Compd.* **2020**, *821*, 153201.

(13) Alexandrova, A. N.; Boldyrev, A. I.; Zhai, H.-J.; Wang, L. S. All-Boron Aromatic Clusters as Potential New Inorganic Ligands and Building Blocks in Chemistry. *Coord. Chem. Rev.* **2006**, *250*, 2811−2866.

(14) Mbarki, M.; St. Touzani, R.; Fokwa, B. P. T. Unexpected synergy between magnetic iron chains and stacked B_6 rings in $Nb_6Fe_{1-x}Ir_{6+x}B_8$. *Angew. Chem., Int. Ed.* **2014**, *53*, 13174−13177.

(15) Sharma, N.; Mbarki, M.; Zhang, Y.; Huq, A.; Fokwa, B. P. T. Structural-Distortion-Driven Magnetic Transformation from Ferro- to Ferrimagnetic Iron Chains in B_6-based $Nb_6FeIr_6B_8$. *Angew. Chem., Int. Ed.* **2018**, *57*, 10323−10327.

(16) Hermus, M.; Yang, M.; Grüner, D.; DiSalvo, F. J.; Fokwa, B. P. T. Drastic change of magnetic interactions and hysteresis through site-preferential Ru/Ir substitution in $Sc_2FeRu_{5-x}Ir_xB_2$. *Chem. Mater.* **2014**, *26*, 1967−1974.

(17) Nagelschmitz, E.; Jung, W. Scandium Iridium Boride $Sc_3Ir_5B_2$ and the Quaternary Derivatives $Sc_2MIr_5B_2$ with M = Be, Al, Si, Ti, V, Cr, Mn, Fe, Co, Ni, Cu, Ga, or Ge: Preparation, Crystal Structure, and Physical Properties. *Chem. Mater.* **1998**, *10*, 3189−3195.
(18) Shankhari, P.; Janka, O.; Poettgen, R.; Fokwa, B. P. T. Rare-Earth-Free Magnets: Enhancing Magnetic Anisotropy and Spin Exchange Toward High-T_C $Hf_2MIr_5B_2$ (M = Mn, Fe). *J. Am. Chem. Soc.* **2021**, *143*, 4205−4212.
(19) May, A. F.; Liu, Y.; Calder, S.; Parker, D. S.; Pandey, T.; Cakmak, E.; Cao, H.; Yan, J.; McGuire, M. A. Magnetic order and interactions in ferrimagnetic $Mn_3Si_2Te_6$. *Phys. Rev. B: Condens. Matter Mater. Phys.* **2017**, *95*, 174440.
(20) Dara, H. K.; Markandeyulu, G. Observation of R-type ferrimagnetism in the intermetallic $Mn_{1.25}Sb$. *J. Magn. Magn. Mater.* **2020**, *505*, 166760.
(21) Bekheet, M. F.; Schlicker, L.; Doran, A.; Siemensmeyer, K.; Gurlo, A. Ferrimagnetism in manganese-rich gallium and aluminium spinels due to mixed valence Mn^{2+}-Mn^{3+} states. *Dalton Trans.* **2018**, *47*, 2727−2738.
(22) Raveau, B.; Caignaert, V.; Pralong, V.; Pelloquin, D.; Maignan, A. A Series of Novel Mixed Valent Ferrimagnetic Oxides with a T_C up to 270 K: $Ca_{1-x}Y_xBaFe_4O_7$. *Chem. Mater.* **2008**, *20*, 6295−6297.
(23) Sheldrick, G. M. A short history of SHELX. *Acta Crystallogr., Sect. A: Found. Crystallogr.* **2008**, *A64*, 112−122.
(24) Huq, A.; Hodges, J. P.; Gourdon, O.; Heroux, L. *Z. Kristallogr. Proc.* **2011**, *1*, 127−135.
(25) Rodriguez-Carvajal, J. *Phys. B* **1993**, *192*, 55−69.
(26) Blöchl, P. E. Projector augmented-wave method. *Phys. Rev. B: Condens. Matter Mater. Phys.* **1994**, *50*, 17953−17979.
(27) Kresse, G.; Joubert, D. From ultrasoft pseudopotentials to the projector augmented-wave method. *Phys. Rev. B: Condens. Matter Mater. Phys.* **1999**, *59*, 1758−1775.
(28) Kresse, G.; Furthmüller, J. Efficient iterative schemes for ab initio total-energy calculations using a plane-wave basis set. *Phys. Rev. B: Condens. Matter Mater. Phys.* **1996**, *54*, 11169−11186.
(29) Hafner, J. Ab-initio simulations of materials using VASP: Density-functional theory and beyond. *J. Comput. Chem.* **2008**, *29*, 2044−2078.
(30) Monkhorst, H. J.; Pack, J. D. Special points for Brillouin-zone integrations. *Phys. Rev. B* **1976**, *13*, 5188−5192.
(31) Perdew, J. P.; Burke, K.; Ernzerhof, M. Generalized gradient approximation made simple. *Phys. Rev. Lett.* **1996**, *77*, 3865−3868.

https://doi.org/10.1021/acs.jpcc.1c02662
J. Phys. Chem. C 2021, 125, 13635−13640